An improved Arbitrary Lagrangian–Eulerian thermal-fluid model by considering powder deposition effects on melting pool during Direct Energy Deposition processes

Yabo Jia, Loïc Jegou, Eric Feulvarch, Yassine Saadlaoui, Valérie Kaftandjian, Thomas Elguedj, Laurent Dubar, Jean-Michel Bergheau

An improved Arbitrary Lagrangian-Eulerian thermal-fluid model by considering powder deposition effects on melting pool during Direct Energy Deposition processes

Yabo Jia[a,b], Loïc Jegou[c,e], Eric Feulvarch[d], Yassine Saadlaoui[d], Valérie Kaftandjian[e], Thomas Elguedj[c], Laurent Dubar[a], Jean-Michel Bergheau[d]

[a]*Univ. Polytechnique Hauts-de-France, CNRS, UMR 8201 - LAMIH - Laboratoire d'Automatique de Mécanique et d'Informatique industrielles et Humaines, F-59313, Valenciennes, France*
[b]*INSA Hauts-de-France, F-59313, Valenciennes, France*
[c]*INSA-Lyon, LaMCoS, UMR 5259 CNRS, Av. Jean Capelle O, Villeurbanne, 69621, France*
[d]*Ecole Centrale de Lyon, CNRS, ENTPE, LTDS, UMR5513, ENISE , Saint-Etienne Cedex 02, 42023, France*
[e]*INSA-Lyon, Laboratoire Vibrations Acoustique, Villeurbanne, 69621, France*

Abstract

Directed Energy Deposition (DED) has emerged notably by offering new possibilities for (re-)manufacturing parts. The multi-phase thermal-fluid models that simulate powder stream deposition are computationally too expensive. The mono-phase Arbitrary Lagrangian-Eulerian (ALE) method are limited in prediction due to exclusion of powder deposition parameters. To address this, we propose an improved 3D mono-phase thermal-fluid model that incorporates powder deposition effects and employs a Moving Thermal-Fluid (MTF) framework to accelerate simulations. Mass, energy, and momentum conservation equations are solved using the finite element method (FEM) and an implicit time integration algorithm, and the ALE method tracks the free surface during deposition. The improved ALE allows considering enthalpy and momentum related to powder deposition through the implementation of new source terms in the energy and momentum conservation equations, leading to more accurate predictions without significantly increasing computing time. Numerical investigations into powder deposition parameters, such as powder distribution, powder enthalpy, and powder mo-

mentum, are conducted to identify their impact on melting pool prediction. The in-situ and ex-situ measurements of the melting pool are also performed to check the efficiency of the proposed model. The applications highlight the importance of incorporating powder stream effects and demonstrate the proposed model's computational efficiency compared to the classical ALE model.

Keywords: multiphysics model, ALE method, Directed Energy Deposition, Thermal-fluid simulation, Powder deposition effects

1. Introduction

Additive manufacturing (AM) has attracted extensive attention and has been developing greatly in the past few decades. The DED process is one of the AM processes, where powders are delivered by the carrier gas flow (such as Argon) onto the substrate or into the melting pool. The manufactured part is printed layer upon layer, thus providing new possibilities for manufacturing parts with complex geometries and different materials. DED processes also present great potential for repair operations. However, the manufactured parts may exhibit various defects, including high roughness, surface defects, cracking, and microstructural heterogeneity. These issues have limited the widespread industrialization of AM technologies. Therefore, both experimental and numerical approaches are employed to gain a better understanding of the physical challenges associated with the process, with the ultimate goal of improving the quality of manufactured parts.

Shah *et al.* [1] experimentally investigated the effects of process parameters and melt pool variables on the surface roughness of the final part and concluded that melt pool disturbance is a vital parameter in determining the surface roughness. Pinkerton *et al.* [2] concluded that the hardness of manufactured samples increased with increasing pulse frequency and had a negative correlation with the pulse duty ratio. Li *et al.* [3] performed a comparative study of melt pool motion, temperature variation, and dendritic morphology of Inconel 718 by applying pulsed-wave laser and continuous-wave laser. Experimental results showed that the pulsed-wave laser resulted in finer columnar dendrites. Recently, Jegou *et al.* [4] developed an in-situ observation platform to observe the evolution of the melting pool during the DED process, and high-quality images of the melting pool have been measured for better controlling the process. In general, the complex multiphysics

and multi-material phenomena occurring during the process make it impossible to capture all the essential information, and the experimental studies can be very expensive considering that the process parameters can be numerous [5]. In this context, numerical methods are alternative solutions and can provide the quantities of interest at all points of the structure, which allow for better understanding of the physical phenomena behind the process and investigating the effect of each process parameter.

The numerical models that solve only heat transfer equations are efficient in terms of computational time. However, these models are not predictive because they do not account for transport phenomena and multiple interactions. The formation of the deposited layer is generally performed by quiet or inactive element techniques [6]. Various numerical techniques, such as the apparent heat capacity method [7], enhanced thermal conductivity approach, adaptive heat source methods [8, 9, 10], and state transformation (powder to compact) [11], have been proposed and applied to improve the numerical prediction quality. However, the capability of heat transfer models is guaranteed only for certain processing parameters, even with the aforementioned numerical techniques, and calibrations are always necessary, which require experimental data and are always time-consuming.

To increase the predictiveness of numerical models, the interactions among the laser beam, powder stream, fluid flow, and heat transfer have been considered and modeled by multi-phase thermal-fluid models. The Computational Fluid Dynamics (CFD) techniques have been exploited to model such processes. The CFD models in DED processes are sophisticated, allowing for the comprehensive modeling of various physical phenomena. Methods such as the level-set [12, 13] and volume-of-fluid (VOF) [14] techniques are employed to track interface evolution during deposition. Various physical phenomena have been investigated by multi-phase models (air, metal), such as the role of the powder stream on heat and fluid flow conditions [15], vaporization phenomena and the impacts of vaporization on powder motion [16], and prediction of inter-track voids [17], etc. More complex modeling frameworks, such as those integrating the Discrete Element Method (DEM) and CFD, have been proposed for DED simulations [18, 19]. These thermal-fluid models offer a unique perspective on modeling real powder particles, providing insights into the physical mechanisms governing powder deposition. Studies have demonstrated that the energy and momentum associated with powder deposition can significantly alter temperature distribution and fluid flow within the melting pool if the quantity of powder absorbed is substantial.

However, one main drawback is that the computational cost is too expensive to simulate several millimeters. Another notable drawback of certain methods, like the VOF technique, is the numerical diffusion of the diffuse interface, leading to a loss of precision and issues with mass conservation [20, 21]. Therefore, a fine mesh should be employed at the interface and its future position, and consequently, the simulations become more computationally expensive. In the aforementioned multi-phase thermal-fluid models, powder particles can be directly modeled, requiring a very fine grid size in the micrometer range. They provide detailed insights into how each powder particle affects the fluid dynamics within the melt pool. Despite efforts to accelerate computations [22], the modeling domain remains limited to several mm^3 with millions of elements.

The ALE-based mono-phase thermal-fluid models allow for the consideration of only the substrate with the deposited layer, thus the ALE-based thermal-fluid model is more computational efficient thanks to two facts: (i) the modeling domain is much smaller in ALE method; (ii) the small viscosity value of air leads to a smaller time step in volume of fluid and level-set methods. Morville *et al.* [23] employed a 2D transient finite element thermal-fluid model to improve the understanding of the phenomena responsible for deleterious surface finish, and the dynamic shape of the molten pool is explicitly tracked by the ALE moving mesh technique. This approach has also been extended to 3D models [24, 25, 26]. Kumar *et al.* [24] studied the effect of melt pool convection and found that Marangoni–Benard convection is dominant in fluid flow dynamics. Wirth *et al.* [25] proposed a physical modeling and predictive simulation of the laser cladding process, where all the input parameters are obtained from measurements without compromising assumptions or calibration. More recently, a local moving thermal-fluid (MTF) framework has been proposed by Jia *et al.* [27]. This method involves solving the exclusive thermal-fluid problem only in a small zone containing the melting pool. Application in part-scale models has been demonstrated in welding and DED, highlighting its computational efficiency. The ALE-based thermal-fluid models are typically developed using the finite element method, where the boundary of the modeling domain represents the interface between the gas and the substrate with deposited layers. Material addition is generally modeled by increasing the volume of elements inside the melting pool. The enthalpy and momentum brought by the powder stream are assumed to be the same as the melting pool. These oversimplifications can sometimes lead to a loss of precision.

In this study, we introduce an improved 3D ALE-based thermal-fluid model for modeling DED processes using the finite element method. This model accounts for surface tension effects (both the 'curvature effect' and the 'Marangoni effect'), buoyancy forces, free surface motion, and mass addition. As the 'keyhole' mode is typically not involved, the free surface is explicitly tracked using the ALE method, ensuring reasonable computing times. Compared to the aforementioned classical ALE-based thermal-fluid model reported in the literature, the powder deposition parameters, including mass, enthalpy, and momentum related to powder particles, are integrated into the model through the addition of new source terms to the conservative governing equations. Meanwhile, the local moving thermal-fluid framework (MTF) is also incorporated into the current model to accelerate the simulations. Numerical investigations are first conducted to explore the impact of powder deposition parameters on fluid dynamics within the melting pool. In the second part, both the proposed model and the classical ALE method are employed to simulate the DED process, and experimental measurements are used to validate the proposed models.

2. Mathematical modelling and methodology

Figure 1 presents the DED process with a co-axial nozzle. A co-axial nozzle moves in the scanning direction over the substrate. The powder particles are delivered by the carrier gas, and a laser beam can heat the in-flight particles and the substrate. In general, the laser beam initializes a melting pool on the substrate. The particles that fall into the molten pool will be melted, and the track layer is created once the molten material solidifies.

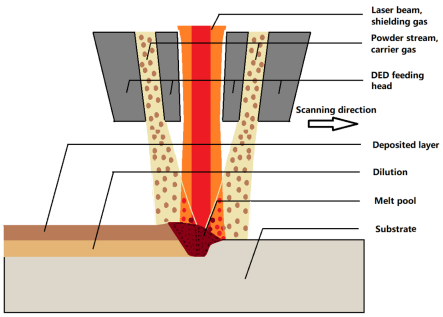

Figure 1: A schematic overview of DED process (co-axial nozzle).

The proposed model considers heat transfer, transport phenomena within the melting pool, and, more importantly, the interactions between powder and laser or powder and melting pool. The following classical assumptions are made [23, 26, 28]:

- The fluid is assumed to be Newtonian, laminar, thermally dilatable, and mechanically incompressible.
- The energy distribution of the laser beam is assumed to be a Gaussian distribution.
- Only the powder falling in the region of the melt pool is melted. The other powder will bounce off from the solidified substrate.
- The pressure evolution related to shielding gas and turbulence is small and can be neglected.
- The powder stream is considered as a continuum medium.

To prepare the input parameters, the powder deposition parameters, such as powder concentration, powder momentum, and the heating effect due to powder-laser interaction, should be identified by numerical methods [29, 30, 31] or experimental measurements [32, 33, 34]. The identification of these parameters is a subject of ongoing research topic, and this aspect will not be detailed here since it is beyond the scope of the current study.

2.1. Moving thermal-fluid (MTF) framework

For a given modeling domain and mesh, solving the thermal-fluid problem discretized by the P1+P1 element requires significantly more computational resources (CPU time, RAM, disk space) compared to solving the heat transfer problem discretized by the P1 linear tetrahedral element. This is due to the higher number of degrees of freedom (DOF) involved in the thermal-fluid problem. The MTF framework [27] aims to accelerate simulations by partitioning the overall modeling domain into two parts: a small moving zone containing the melt pool, where the thermal-fluid problem is solved, and a considerably larger part where the heat transfer problem is addressed. The domain is meshed with linear tetrahedral elements. The thermal-fluid computational zone is defined by a cubic box co-moving with the laser beam. Table 1 presents the governing equations in each computational zone, and Table 2 provides a summary of the boundary conditions involved. More details about MTF framework can be found in work of JIA *et al.* [27].

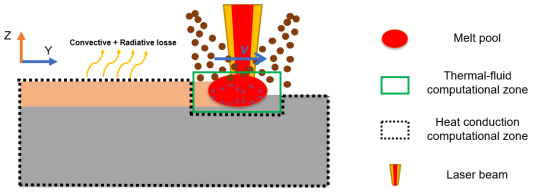

Figure 2: Application of MTF framework to DED simulations.

Table 1: Governing equations in different computational zone.

	Thermal-fluid computational zone (P1+P1)	Heat conduction computational zone (P1)
Governing equations	$\operatorname{div}\mathbf{v} + \frac{\dot{\rho}}{\rho} = 0$ [(1)] $\rho\left(\frac{\partial H}{\partial t} + \mathbf{v}\cdot\operatorname{grad} H\right) - \operatorname{div}(\lambda \operatorname{grad} T) - Q = 0$ [(2)] $\rho\left(\frac{\partial \mathbf{v}}{\partial t} + \operatorname{grad}\mathbf{v}\cdot\mathbf{v}\right) = -\operatorname{grad} p + \operatorname{div}\mathbf{s} + \mathbf{f_v}$ [(3)]	$\rho\left(\frac{\partial H}{\partial t}\right) - \operatorname{div}(\lambda \operatorname{grad} T) = 0$

[(1)] mass conservation equation, $\mathbf{v}$ the velocity, $\frac{\dot{\rho}}{\rho}$ volume change.

[(2)] energy conservation equation, H the specific enthalpy, Q the heat source to simulate heating effects, λ thermal conductivity.

[(3)] momentum conservation equation, p being the fluid pressure, $\mathbf{s}$ stress deviator, $\mathbf{f_v}$ represents the volume forces.

Table 2: The associated boundary conditions.

Zone / Physics	Thermal-fluid computational zone	Heat conduction computational zone
Heat transfer	$\lambda\cdot\nabla T\cdot\mathbf{n} = -h_c(T-T_0) - \varepsilon\sigma(T^4 - T_0^4)$ [(1)]	$\lambda\cdot\nabla T\cdot\mathbf{n} = -h_c(T-T_0) - \varepsilon\sigma(T^4 - T_0^4)$ [(1)]
Fluid dynamics	Surface tension: $\sigma_{\text{surface}} = \gamma\mathbf{1}_S$ [(2)]	NO
ALE moving mesh	Free surface: $V(t) = \left(\mathbf{v}\cdot\mathbf{n} + \frac{\dot{a}}{\rho}\right)\cdot\mathbf{n}_i$ [(3)]	NO

[(1)] heat convective and radiative losses. Temperature should be in Kelvin.

[(2)] curvature and Marangoni effects, γ surface tension, $\mathbf{1}_S$ local surfacic 2D unit tensor.

[(3)] free surface moving equation, $\mathbf{v}$ the velocity given by momentum conservation equation, $\frac{\dot{a}}{\rho}$ the free surface motion due to surfacial mass addition.

2.2. Improved ALE thermal-fluid model

As the fluid is thermally dilatable and mechanically incompressible, the volume change only depends on the temperature evolution. In the mechanics of fluid, the stress tensor can be expressed as:

$$\begin{aligned} \boldsymbol{\sigma} &= \mathbf{S} - p\mathbf{I} = 2\mu\mathbf{D}_m - p\mathbf{I} \\ \mathbf{D}_m &= \mathbf{D} + \tfrac{\dot{\rho}}{3\rho}\mathbf{I} \end{aligned} \tag{1}$$

where p is the pressure, μ is the viscosity of fluid, $\mathbf{D}$ is the Eulerian strain rate ($\mathbf{D} = \frac{1}{2}\left(\operatorname{grad}\mathbf{v} + (\operatorname{grad}\mathbf{v})^{\top}\right)$), $\mathbf{D_m}$ is the mechanical strain rate. The variations of ρ are only due to the thermal dilation effects, and $\frac{\dot{\rho}}{\rho} \cong -3\alpha\dot{T}$, where α is thermal expansion coefficient. The material is supposed to be mechanically incompressible.

Figure 3 focuses on some details in modeling the region of the melt pool. Let us consider a bounded modeling domain Ω with boundary $\partial\Omega$. Only the powder falling in the region of the melt pool ($\partial\Omega_{\dot{a}}$) is melted, which creates a new track after cooling. It's important to note that the powder stream introduces not only mass addition, which can create new tracks, but also energy (powder heated by the laser beam) and momentum (powder impinging into the melting pool with initial velocity) perturbations within the melt pool across the interface. In general, the energy and momentum associated with the powder stream are ignored in classical ALE thermal-fluid models due to oversimplifications. Some aforementioned work [15, 18] shows that the energy and momentum related to the powder stream can significantly influence the fluid dynamics in the melt pool and thus the final track shape after cooling. Therefore, it is important to incorporate the powder deposition effects in ALE thermal-fluid models to benefit from their computational efficiency.

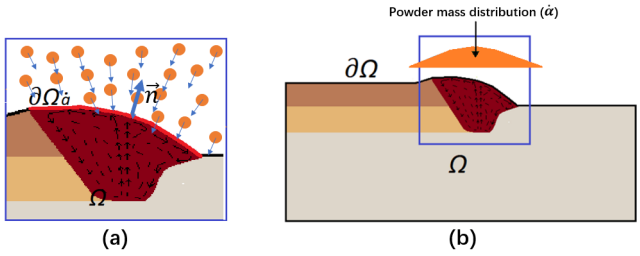

Figure 3: (a) powder deposition $\dot{a}$ through free surface of the molten pool $\Omega_{\dot{a}}$, (b) modeling domain Ω and its boundary $\partial\Omega$.

To accurately calculate the fluid flow behavior and free surface evolution without significantly increasing the complexity of the thermal-fluid model, the present study introduces an improved ALE thermal-fluid model. This model aims to reveal the complex physical phenomena of DED processes, including fluid dynamics in the melt pool, heat transfer in solid and fluid states, free surface evolution, laser-substrate interaction, melting, and solidification processes. The mass addition is performed by introducing an additional velocity at the free surface ($\partial\Omega_{\dot{a}}$), which depends on powder distribution in space. The energy and momentum associated with the powder stream will be incorporated into the set of governing equations by adding additional source terms, which will lead to a more accurate and physically realistic prediction of fluid dynamics in the molten pool and final track shape. Since the powder deposition effects (mass, enthalpy, momentum) directly impact the surface of the melting pool, all these effects will be integrated through the 2D element of the free surface in the corresponding governing equations.

In the current study, mixed P1+P1 tetrahedral elements are used for the discretization of fluid elements. The finite element formulation of the fluid problem relies on a mixed velocity–pressure ($\mathbf{v}$, p) variational formulation [35]. The coupled heat transfer and fluid flow dynamic problems are governed by the following three equations:

Variational formulation of mass conservation

The weak formulation of mass balance is written :

$$\int_\Omega p^* \left(\mathrm{div}(\mathbf{v}) + \frac{\dot{\rho}}{\rho}\right) dv = 0 \tag{2}$$

$$\text{with boundary condition : } \rho\mathbf{v}\cdot\mathbf{n} = \dot{a} \text{ on the free surface } \Omega_{\dot{a}}.$$

where $\dot{a}$ represents the powder concentration distribution in space. More details can be found in section 2.4.

Variational formulation of momentum conservation (Navier–Stokes equations)

The variational formulation of conservation of momentum (Navier-Stokes equations) takes its form:

$$
\begin{aligned}
&- \int_\Omega \mathbf{v}^* \rho \left(\tfrac{\partial \mathbf{v}}{\partial t} + \mathrm{grad}(\mathbf{v}) \cdot \mathbf{v} \right) d\tau - \int_\Omega \mathbf{D}^* : 2\mu \mathbf{D}_m d\tau + \int_\Omega \mathrm{div}\left(\mathbf{v}^*\right) p d\tau \\
&+ \int_{\partial\Omega} \mathbf{v}^* \cdot \varphi^d ds + \mathbf{S_{vol}} + \mathbf{S_{suf}} + \mathbf{S_{mom}} = 0
\end{aligned}
\tag{3}
$$

where $\boldsymbol{\varphi}^d$ prescribes surface force (equal to $\boldsymbol{\sigma} \cdot \mathbf{n}$) on $\partial\Omega_T$. $\mathbf{S_{vol}}$ represents the source term of volume force. $\mathbf{S_{suf}}$ is the surface tension effects (corresponding to $\mathbf{f_v}$ in Table 1). $\mathbf{S_{mom}}$ is the newly implemented source term to consider the momentum related to the powder stream.

In the fluid flow simulation, the source term $\mathbf{S_{vol}}$ can be used to describe the buoyancy forces and is expressed as follows (Eq. 4):

$$
\mathbf{S_{vol}} = \int_\Omega \mathbf{v}^* \cdot \mathbf{f_v} d\tau = \int_\Omega \mathbf{v}^* \cdot [\rho_0 (1 - \alpha(T - T_0))\mathbf{g}] d\tau \tag{4}
$$

with ρ_0 being the material density at the reference temperature T_0, $\mathbf{g}$ the gravitational acceleration.

Since surface tension effects play an important role in fluid dynamics in the molten pool [36, 37, 38], it is necessary to take these effects into account. Different forms of classical techniques have been proposed in finite-element codes [39, 40]. In the current study, we adopt an efficient approach based on the equivalence between the effects of surface tension and those of a fictitious stressed membrane bonded to the free surface [41]. (Eq. 5):

$$
\mathbf{S_{suf}} = \int_{\partial\Omega_{skin}} \mathbf{D}^* : \tau ds \tag{5}
$$

To derive the source term $\mathbf{S_{mom}}$, we start with a volumetric mass addition term $\dot{A}$ (unit: $\mathrm{kg} \cdot \mathrm{s}^{-1} \cdot \mathrm{m}^{-3}$) instead of the surface mass addition term $\dot{a}$ (unit: $\mathrm{kg} \cdot \mathrm{s}^{-1} \cdot \mathrm{m}^{-2}$). In this case, the global momentum balance is now written for any material domain Ω (Eq. 6):

$$
\begin{aligned}
\frac{d}{dt}\left(\int_\Omega \rho \mathbf{v} d\tau \right) &= \int_\Omega \mathbf{f_v} d\tau + \int_{\partial\Omega} \boldsymbol{\varphi}^d ds + \int_\Omega \dot{A} \mathbf{v}_{\mathrm{add}} d\tau \\
&= \int_\Omega \left(\mathbf{f_v} + \dot{A} \mathbf{v}_{\mathrm{add}} \right) d\tau + \int_{\partial\Omega} \boldsymbol{\sigma} \cdot \mathbf{n} ds
\end{aligned}
\tag{6}
$$

with $\mathbf{f_v}$, the force volume density representing the external actions, and $\boldsymbol{\varphi}^d$, the stress vector representing the areal stress density associated with the contact actions between Ω and the rest of the medium. $\mathbf{v}_{add}$ represents the

velocity vector of the powder stream. $\boldsymbol{\sigma}$ is the Cauchy stress tensor, and $\mathbf{n}$ is the outgoing direction normal to $\partial\Omega$.

By integrating mass conservation into the left-hand sides of Eq. 6, we currently obtain :

$$\begin{aligned}\frac{d}{dt}\left(\int_\Omega \rho\mathbf{v}d\tau\right) &= \int_\Omega \mathbf{v}\left(\frac{d\rho}{dt}+\rho\,\mathrm{div}(\mathbf{v})\right)d\tau + \int_\Omega \rho\left(\frac{\partial\mathbf{v}.}{\partial t}+\mathrm{grad}\,\mathbf{v}\cdot\mathbf{v}\right)d\tau \\ &= \int_\Omega \dot{A}\mathbf{v}d\tau + \int_\Omega \rho\left(\frac{\partial\mathbf{v}.}{\partial t}+\mathrm{grad}\,\mathbf{v}\cdot\mathbf{v}\right)d\tau\end{aligned} \tag{7}$$

By applying the divergence theorem to transform surface integrals into volume integrals, the final global momentum balance is finally written :

$$\rho\left(\frac{\partial\mathbf{v}}{\partial t}+\mathrm{grad}\,\mathbf{v}\cdot\mathbf{v}\right)d\tau - \left(\mathrm{div}\boldsymbol{\sigma}+\mathbf{f_v}+\dot{A}\left(\mathbf{v}_{\mathrm{add}}-\mathbf{v}\right)\right)d\tau = 0 \tag{8}$$

To calculate an equivalent boundary condition applied on $\partial\Omega_{\dot{a}}$, for a given point P on the free surface $\partial\Omega_{\dot{a}}$, we consider an infinitely small surface dS centered on this point and a volume dV corresponding to the surface dS extruded inward from Ω through a thickness of e (see Fig. 4).

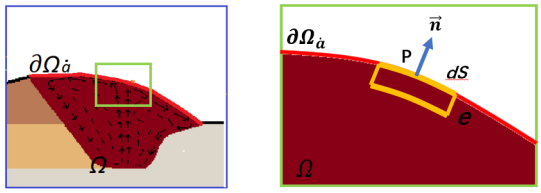

Figure 4: Calculation of equivalent boundary condition for representing momentum $\mathbf{S_{mom}}$.

In reality, the mass addition is performed by a surface mass flux $\dot{a}$ through the free surface of the molten pool $\partial\Omega_{\dot{a}}$. Let's distribute this surface mass flow in the volume dV, and the relationship between the volume mass flow and surface mass flow can be expressed as $\dot{A} = \frac{\dot{a}}{e}$. Thus, the integration of partial differential equations governing the conservation of momentum (Eq. 8) in the volume dV is finally written as (Eq. 9):

$$\int_{dV}\left(\rho\left(\frac{\partial \mathbf{v}\cdot}{\partial t}+\mathrm{grad}\mathbf{v}\cdot\mathbf{v}\right)-\mathrm{div}\,\sigma-\mathbf{f_v}-\frac{\dot{a}}{e}\left(\mathbf{v}_{\mathrm{add}}-\mathbf{v}\right)\right)d\tau=$$
$$\left(\rho\left(\frac{\partial \mathbf{v}}{\partial t}+\mathrm{grad}\mathbf{v}\cdot\mathbf{v}\right)-\mathbf{f_v}\right)edS-\dot{a}\left(\mathbf{v}_{\mathrm{add}}-\mathbf{v}\right)dS-\int_{dV}\mathrm{div}\boldsymbol{\sigma}d\tau=0 \tag{9}$$

By applying the divergence theorem on the term $\int_{dV}\mathrm{div}\,\boldsymbol{\sigma}d\tau$ then letting the thickness e tend to 0, one can deduce (Eq. 10):

$$\boldsymbol{\sigma}\cdot\mathbf{n}=\dot{a}\left(\mathbf{v}_{\mathrm{add}}-\mathbf{v}\right)\ \text{ on surface } \partial\Omega_{\dot{a}} \tag{10}$$

Finally one has (Eq. 11):

$$\mathbf{S_{vol}}=\int_{\partial\Omega_{\dot{a}}}\mathbf{v}^*\cdot\dot{a}(\mathbf{v}_{\mathrm{add}}-\mathbf{v})ds \tag{11}$$

The final weak formulation of conservation of momentum is formulated as follows (Eq. 12):

$$\begin{aligned}&-\textstyle\int_\Omega\mathbf{v}^*\rho\left(\frac{\partial\mathbf{v}}{\partial t}+\mathrm{grad}(\mathbf{v})\cdot\mathbf{v}\right)d\tau-\int_\Omega\mathbf{D}^*:2\mu\mathbf{D}_m d\tau+\int_\Omega\mathrm{div}\left(\mathbf{v}^*\right)pd\tau\\&+\textstyle\int_{\partial\Omega}\mathbf{v}^*\cdot\boldsymbol{\varphi}^d ds+\int_\Omega\mathbf{v}^*\cdot\mathbf{f_v}d\tau+\int_{\partial\Omega_{skin}}\mathbf{D}^*:\boldsymbol{\tau}ds\\&+\textstyle\int_{\partial\Omega_{\dot{a}}}\mathbf{v}^*\cdot\dot{a}(\mathbf{v}_{\mathrm{add}}-\mathbf{v})ds=0\end{aligned} \tag{12}$$

Variational formulation of energy balance

Similarly to the derivation of momentum conservation equation, the global energy balance equation for any material domain Ω is written (Eq. 13) :

$$\begin{aligned}\frac{d}{dt}\left(\int_\Omega\rho H d\tau\right)&=\int_\Omega s d\tau-\int_{\partial\Omega}\varphi\cdot\mathbf{n}ds+\int_\Omega\dot{A}H_{\mathrm{add}}d\tau\\&=\int_\Omega\left(s+\dot{A}H_{\mathrm{add}}\right)d\tau+\int_{\partial\Omega}\lambda\mathrm{grad}\,T\cdot\mathbf{n}ds\end{aligned} \tag{13}$$

with s, the volumetric heat source. H represents the local enthalpy of volume Ω and φ, the heat flux density vector. φ is related to the temperature gradient by Fourier's law: $\varphi=-\lambda\mathrm{grad}\,\mathbf{T}$.

The term $\int_\Omega \dot{A} H_{add} d\tau$ in Eq. 13 represents the energy input associated with the mass addition, with H_{add} the enthalpy of the powder stream which depends on the temperature of powder stream.

By integrating mass addition ($\dot{A}$) into the left-hand sides of Eq. 13, we currently obtain Eq. 14:

$$\begin{aligned}\frac{d}{dt}\left(\int_\Omega \rho H d\tau\right) &= \int_\Omega H\left(\frac{d\rho}{dt} + \rho \operatorname{div}(\vec{v})\right) d\tau + \int_\Omega \rho\left(\frac{\partial H}{\partial t} + \mathbf{v}\cdot \operatorname{grad} H\right) d\tau \\ &= \int_\Omega \dot{A} H d\tau + \int_\Omega \rho\left(\frac{\partial H}{\partial t} + \mathbf{v}\cdot \operatorname{grad} H\right) d\tau\end{aligned} \tag{14}$$

By applying the divergence theorem to transform surface integrals into volume integrals, the final global energy balance is finally written (Eq. 15):

$$\rho\left(\frac{\partial H}{\partial t} + \mathbf{v}\cdot \operatorname{grad} H\right) - \operatorname{div}(\lambda \operatorname{grad} T) - s - \dot{A}\left(H_{\text{add}} - H\right) = 0 \tag{15}$$

We perform the integration of partial differential equations governing the conservation of momentum (Eq. 15) in the volume dV (Fig. 4), and we have (Eq. 16) :

$$\begin{aligned}&\int_{dV} \rho\left(\frac{\partial H}{\partial t} + \mathbf{v}\cdot \operatorname{grad} H\right) - \operatorname{div}(\lambda \operatorname{grad} T) - s - \dot{A}\left(H_{\text{add}} - H\right) d\tau = \\ &\left(\rho\left(\frac{\partial H}{\partial t} + \vec{v}\cdot \operatorname{grad} H\right) - s\right) e dS - \dot{A}\left(H_{\text{add}} - H\right) dS - \int_{dV} \operatorname{div}(\lambda \operatorname{grad} T) d\tau = 0\end{aligned} \tag{16}$$

By applying the divergence theorem on the term $\int_{dV} \operatorname{div}(\lambda \operatorname{grad} T) d\tau$ then letting the thickness e tend to 0, one can deduce (Eq. 17) :

$$\lambda \frac{\partial T}{\partial n} = \dot{a}\left(H_{\text{add}} - H\right) \quad \text{on surface } \partial\Omega_{\dot{a}} \tag{17}$$

Thus the final variational formulation of energy balance can be expressed as :

$$\begin{aligned}&-\int_\Omega T^* \rho\left(\tfrac{\partial H}{\partial t} + \mathbf{v}\cdot \operatorname{grad} H\right) d\tau - \int_\Omega \operatorname{grad} T^* \cdot \lambda \operatorname{grad} T d\tau + \int_\Omega T^* s d\tau \\ &\qquad + \int_{\partial\Omega} T^* q ds + \int_{\partial\Omega_{\dot{a}}} T^* \dot{a}\left(H_{\text{add}} - H\right) ds = 0\end{aligned} \tag{18}$$

2.3. ALE moving mesh

After solving the global system (thermal-fluid and heat transfer), the temperature and velocity fields at nodes are determined. To track the free surface evolution, the ALE moving mesh technique is employed to account for the fluid dynamic effects as well as the mass addition. Therefore, the displacement corresponding to the free surface evolution depends on both the velocity field calculated from the momentum conservation equation and surface mass addition ($\dot{a}$). As it has been assumed that only the powder falling into the melt pool can be melted, which means that only the nodes processing a temperature beyond the melting temperature (T_f) can include the term $\frac{\dot{a}}{\rho}$. Finally, the displacement at node i can be expressed as (Eq. 19):

$$\Delta \mathbf{U}_i = \left(\mathbf{v} \cdot \mathbf{n} + \frac{\dot{a}}{\rho} \right) \Delta \mathrm{t} \cdot \mathbf{n} \tag{19}$$

where $\Delta \mathbf{U}_I$ represents the displacement of the node i for a given time step Δt, and ρ is the density of powder particles. $\mathbf{v}$ is the velocity field calculated from the momentum conservation equation.

Figure 5 illustrates the strategy for updating nodal position during ALE procedure, two temperature criteria ($\mathrm{T_{melting}}$ and $\mathrm{T_{ALE}}$) have been defined ($\mathrm{T_{melting}}$ greater than $\mathrm{T_{ALE}}$). To ensure a good mesh quality, the elastic domain ($\mathrm{T_{element}} > \mathrm{T_{ALE}}$) for reposition of nodes is larger than the melting pool since the mass addition can be important.

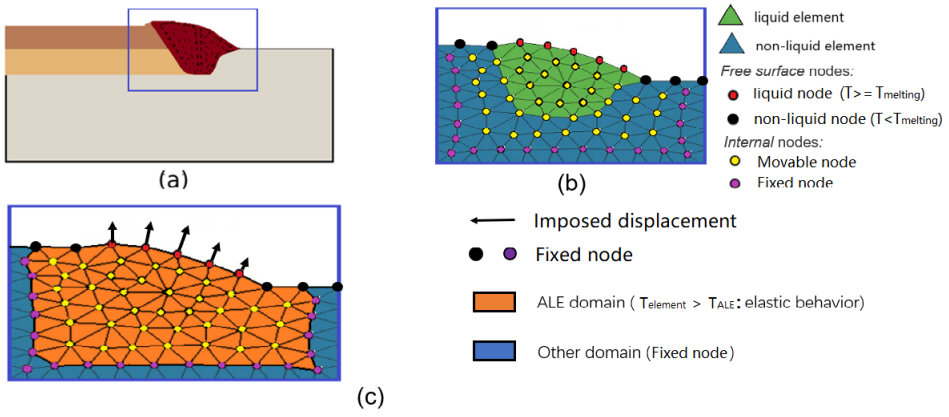

Figure 5: Illustration of ALE procedure for updating the nodal position.

2.4. Proposed global resolution schema

Figure 6 presents the proposed global resolution schema, which allows better appreciation of the proposed efficient resolution schema. This diagram illustrates the interactions between the sub-sections, including the MTF framework, improved governing equations, and the ALE moving mesh.

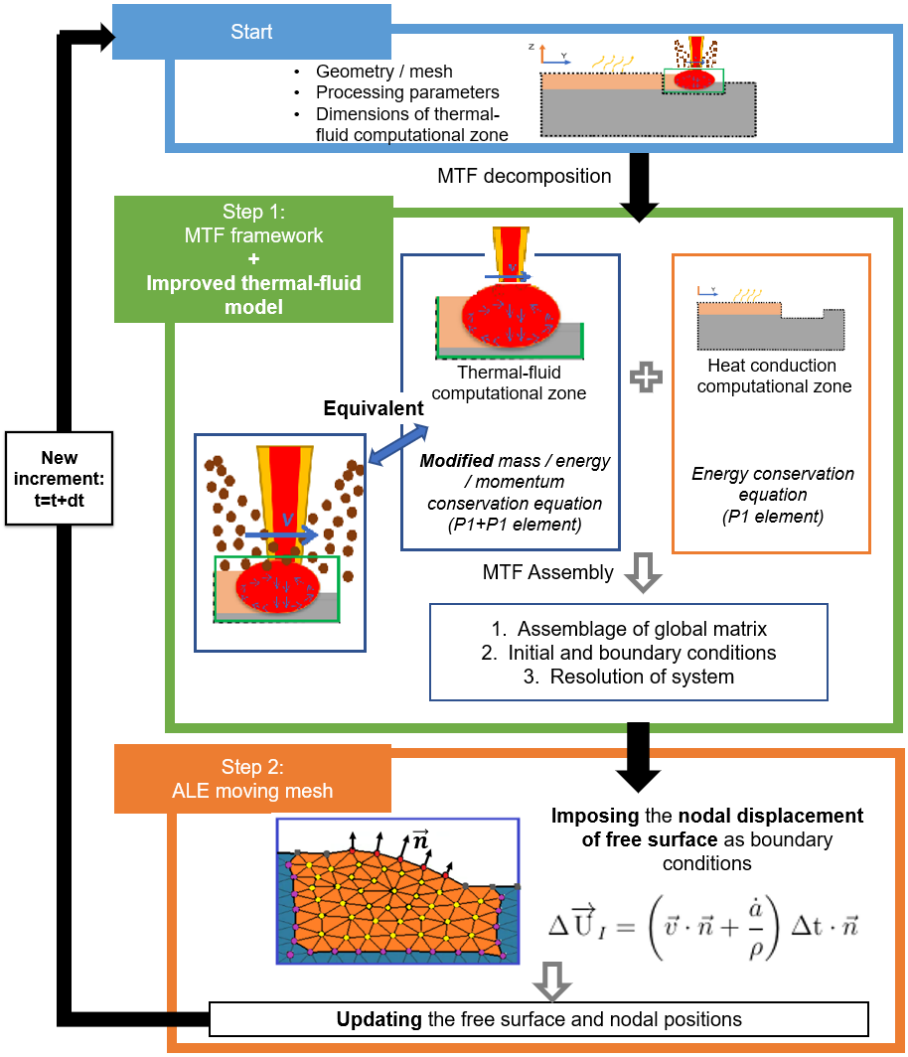

Figure 6: Overview of proposed global resolution procedure.

3. Numerical case studies

In this section, two kinds of numerical tests in DED simulations are presented to assess the efficiency of the proposed model. Thanks to the implementation of source terms in the thermal-fluid governing equations, different powder deposition parameters can be efficiently accounted for by the proposed ALE method for the first time, and the effects of these parameters (powder flux distribution, enthalpy of powder flux, velocity of powder particles) will be investigated numerically. These studies contribute to a better understanding of the DED process and further accelerate the optimization of fabrication parameters.

The first example involves a fixed nozzle and laser in space, and temperature-independent material properties are used to simplify the physical model and comparisons. Since this analysis focuses solely on the numerical models, the physical models (material properties) are of less importance, as the material and operational parameters can vary. Our primary interest is in observing the trends in melting pool size when different powder deposition parameters are employed, highlighting the significance of considering these parameters in numerical models. Using constant material properties simplifies the numerical resolution as well as the comparison of numerical results, particularly regarding the predicted melt pool size, allowing us to better isolate the direct effects of powder deposition parameters. In this case study, numerous powder deposition parameters will be investigated in detail. The effects of each parameter will be quantified through comparisons of numerical results, such as temperature evolution and melt pool size.

The second application involves simulating the DED process with a moving nozzle and laser beam, where temperature-dependent material properties are employed. The simulation case is supposed to be more realistic than the first one. Both the classical ALE thermal-fluid model and the improved ALE thermal-fluid model will be utilized to simulate the same case. Comparisons of the numerical results will underscore the importance of considering powder deposition parameters in achieving more accurate simulations. The developments are integrated into FE software SYSWELD^{TM} version 2023 [42], and the pre/post-treatment are prepared by Visual-Environment [43] in this study. Certainly, the idea can be extended and implemented in other software. For simplification, the improved ALE-based thermal-fluid model will be called "Improved ALE" in the sequel.

3.1. Fixed nozzle and laser beam

Figure 7 shows the configuration and mesh of the test case with a fixed nozzle and laser beam, with some basic dimensions provided. This numerical test includes about 17k nodes and 90k 3D elements, and the smallest element dimension is 100 μm in the powder deposition zone. The energy distribution of the laser beam and powder deposition parameters (mass concentration, enthalpy, momentum) are simplified and defined by a constant value or a spatial-temporal function. All external surfaces can exchange freely with the air.

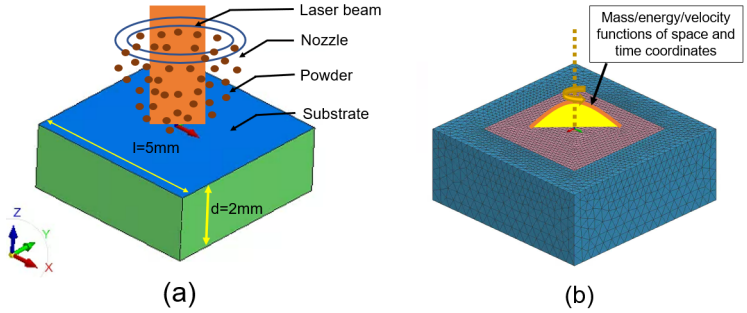

Figure 7: Configuration and mesh of test case with fixed nozzle and laser beam.

The laser beam is projected in the z direction, and the center of the laser beam coincides with the origin of the coordinate system. As the numerical results will not be validated against the experiments, the intensity of laser power is described by a Gaussian function as:

$$Q(x,y) = \frac{\eta B P}{\pi * R^2} * \exp(-\frac{B * (x^2 + y^2)}{R^2}) \tag{20}$$

where $Q(x,y)$ is the laser power intensity distribution at Gauss point that depends on the relative position (x,y) compared to the center of the laser beam (See Figure 7); R, B, η, P represent the radius of the laser beam, coefficient of Gaussian distribution, coefficient of absorption, and the power of the laser beam. The exact parameters are detailed in Table 3.

In the literature, the powder concentration depends on the choice of deposition distance between the surface of the substrate and the nozzle. In general, the converging point is selected to improve the catching efficiency by the melt pool, and experience shows that the powder concentration at the converging point follows a Gaussian distribution [44]:

Table 3: Parameters of the laser beam.

Power (P)	Radius (R)	Absorptivity (η)	Gaussian function (B)
Watt	m	-	-
300	0.001	0.4	1

$$\dot{a}(r) = \frac{C_p * \dot{m}}{\pi * r_p^2} * e^{(-\frac{C_p * r^2}{r_p^2})} \tag{21}$$

where C_p, r, r_p, $\dot{m}$ are the Gaussian parameters, distance from the deposition center in the plane X-Y, effective radius of powder deposition, and mass deposition rate (kg/s), respectively. Table 4 shows the powder concentration parameters that are employed in the numerical test.

Table 4: Powder concentration parameters in fixed nozzle case.

Mass flux ($\dot{m}$)	Radius (r_p)	Gaussian parameter (C_p)
kg/s	m	-
0.00013	0.001	1

The temperature of powder stream can be defined by a constant value or a time-space function as the powder concentration, and this parameter can be measured experimentally or simulated. In the current tests, a constant value T_p that represents the average temperature is used for simplification.

To consider the effect of momentum (a product between mass and velocity), the velocity can be defined by a vector or a time-space function, which should be determined experimentally or numerically. Same as the temperature, a constant and uniform vector $v*(0, 0, 1)$ is used to describe the velocity of powder flow (the coordinate system is shown in Figure 7).

Table 5: Material properties used in first test [45, 46].

Density	Specific heat	Thermal conductivity	Surface tension	Surface tension gradient	Dynamic viscosity (liquid)
kg/m^3	J/(kg K)	W/mK	N/m	N/(m T)	Pa s
8000	450	14.7	1.51	$2.28*10^{-4}$	0.007

For simplifying the complexity of model, table 5 presents the constant material properties of 316L in the first case. The melting temperature is of

1450 °C. It's important to note that dynamic viscosity needs to be defined based on the element state (liquid, non-liquid). The non-liquid elements are assigned a larger viscosity value (about 100 Pa s) to better simulate the solid state. The surface tension ($\boldsymbol{\gamma}$) value at melting temperature (T_m) is given in Table 5, and the surface tension can be written as $\gamma(T) = \gamma + (T - T_m) \cdot d\gamma$.

To investigate the importance of powder deposition parameters, all the simulations are performed in two steps. Firstly, a thermal-fluid simulation without powder deposition for 0-0.25 s, and an initial melting pool is created. Secondly, the powder deposition starts at 0.25 s for a duration of 0.1 s. Both classical ALE method and improved ALE method are employed. The classical ALE method makes strong assumptions that the powder absorbed has the immediately same velocity and temperature as the melting pool, and the powder deposition parameters are ignored. Thus the melting pool predicted by the classical ALE method is generally much deeper and larger, in general, a lower non physical laser absorptivity should be calibrated to have a better approximation. The melting pool simulated by classical ALE method is shown in Figure 8.

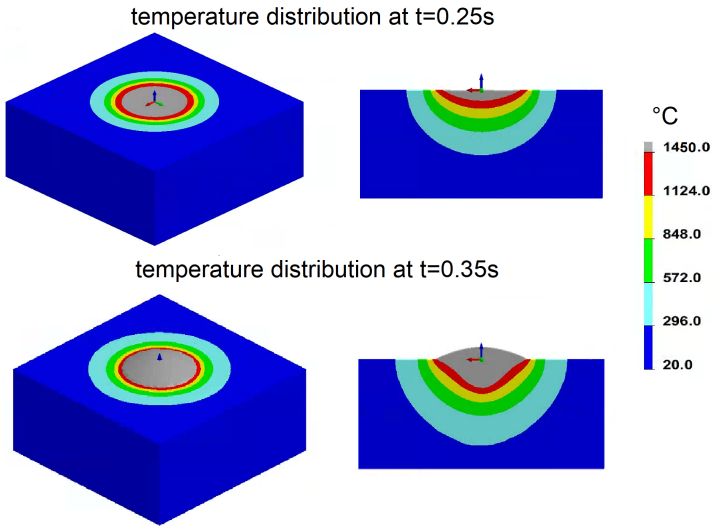

Figure 8: Temperature distribution and melting pool at the beginning (t=0.25 s) and end (t=0.35 s) of powder deposition simulated by Classical ALE.

The simulation with the improved ALE method is performed with an average powder temperature of $T_p = 1000$ °C and a powder flow velocity of $v = -1$ m/s in axis z. The temperature distribution at $t = 0.35$ s is presented

in Figure 9. The melting pool predicted by the improved ALE method is smaller than that of the classical ALE method. This can be explained by the fact that the unmelted powder (at 1000 °C) absorbed can cool down the melting pool. Therefore, a smaller melting pool will subsequently absorb less powder, resulting in a smaller height and length of the melting pool simulated by the improved ALE method compared to that given by the classical ALE method.

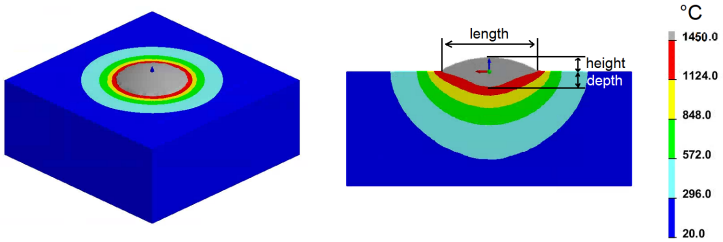

melting pool size simulated by classical ALE and improved ALE

	length (mm)	height (mm)	depth (mm)
Classical ALE	1.83	0.23	0.52
Improved ALE	1.72	0.22	0.28

Figure 9: Temperature distribution and melting pool at t=0.35 s simulated by improved ALE.

Table 6: Different powder deposition parameters.

Analysis	ID	Gaussian (C_p)	Temperature (T_p)	Velocity (V_p)
Powder concentration	C-0.5	0.5	1000°C	1 m/s
	C-1	1	1000°C	1 m/s
	C-3	3	1000°C	1 m/s
Powder temperature	T-1	3	800°C	1 m/s
	C-3	3	1000°C	1 m/s
	T-3	3	1500°C	1 m/s
Powder velocity	C-3	3	1000°C	1 m/s
	V-2	3	1000°C	4 m/s
	V-3	3	1000°C	8 m/s

Turning now to the investigation of powder deposition parameters, we examine the effects of powder concentration, powder temperature, and powder velocity (see Table 6). It should be noted that the Gaussian parameter (C_p) plays an important role, directly modifying the quantity of powder absorbed

by the melting pool, and consequently affecting the associated enthalpy and momentum. Therefore, the powder concentration parameter is the most dominant.

The first investigation is the effect of powder concentration on temperature distribution and melting pool. To individually investigate the powder concentration effect, the assumption here is that the laser power reaching at the surface will not depend on the powder concentration (without evolution of laser attenuation).

With an increase in powder concentration, the initial melting pool presented in Figure 10 will absorb more powder. Therefore, the simulation case with C=3 exhibits the highest absorption among all the simulations. Another interesting finding is that the depth in case C=3 is the lowest, which confirms that unmelted powder reduces the depth of the melting pool, leading to smaller penetration. Meanwhile, the length of the melting pool in case C=3 becomes larger, which may be explained by the fact that the melting liquid tends to elongate to achieve more stability. To highlight the effect of powder temperature and powder velocity on the melting pool, a Gaussian parameter of 3 is taken for the following analysis.

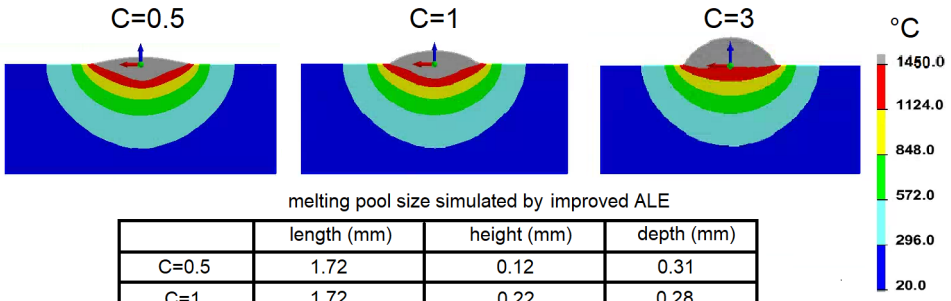

melting pool size simulated by improved ALE

	length (mm)	height (mm)	depth (mm)
C=0.5	1.72	0.12	0.31
C=1	1.72	0.22	0.28
C=3	1.80	0.49	0.01

Figure 10: Investigation the effect of powder concentration on the temperature distribution and melting pool at t=0.35 s simulated by improved ALE.

Figure 11 provides a comparison of the melting pool with different powder temperatures predicted by the proposed model. The higher the powder temperature, the larger and deeper the melting pool becomes. In contrast, the height of the melting pool becomes smaller with an increase in the powder temperature. This may be explained by the fact that the quantity of powder absorbed by the melting pool remains almost the same; therefore, a larger melting pool will lead to a smaller melting height.

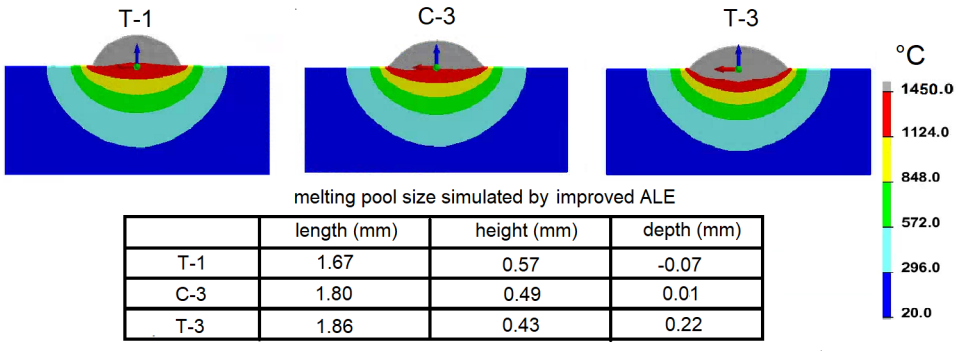

melting pool size simulated by improved ALE

	length (mm)	height (mm)	depth (mm)
T-1	1.67	0.57	-0.07
C-3	1.80	0.49	0.01
T-3	1.86	0.43	0.22

Figure 11: Investigation the effect of powder temperature of the temperature distribution and melting pool at t=0.35 s simulated by improved ALE.

The last comparison concerns the effect of powder velocity (Figure 12). Since the gradient of surface tension is positive, the fluid circulates from the border to the center. Therefore, one can imagine that deposited powder could accelerate the circulation, which may increase the depth and length of the melting pool, consequently leading to a smaller height of the melting pool.

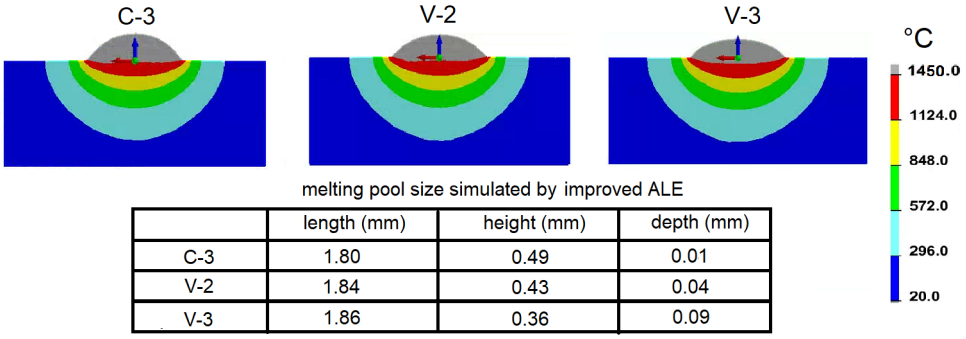

melting pool size simulated by improved ALE

	length (mm)	height (mm)	depth (mm)
C-3	1.80	0.49	0.01
V-2	1.84	0.43	0.04
V-3	1.86	0.36	0.09

Figure 12: Investigation the effect of powder velocity of the temperature distribution and melting pool at t=0.35 s simulated by improved ALE.

The effect of powder concentration, powder temperature, and powder velocity on the melting pool are investigated individually. Powder concentration has the most significant and direct effect on the temperature and consequently on the dimensions of the melting pool. Powder temperature has a direct impact on the melting pool; in general, the powder will cool down the melting pool during the DED process. Powder velocity can modify

the local mass transfer effect in the melting pool, thus changing the temperature. However, the effect of powder temperature and velocity depends strongly on the quantity of powder absorbed.

3.2. Mobile nozzle and laser beam

3.2.1. Experiments set-up

Figure 13 presents the experimental setup, which has been developed to perform DED processes with in-situ observation [4]. The RGB camera captures the size of the melting pool in-situ on the upper surface. An optical microscope is employed after the process to determine the width and depth of the melt pool, as well as the fusion profile.

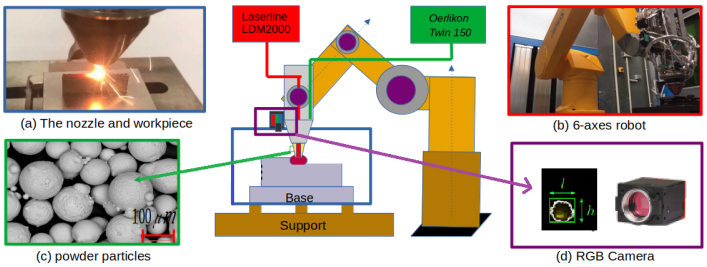

Figure 13: Schematic view of the experimental setup.

Table 7 summarizes all the devices applied in the experimental setup. The samples are produced by a water-jet process, which allows increasing the absorptivity of laser.

Table 7: Devices of the experimental setup.

Parameters	Values
Laser and optics	Laserline LMD2000, Spot size: 1.4 mm
Nozzles	Precitec - ZM YC50 DIS II Carrier Gas (inner)
	Precitec - ZM YC50 DAS 0.5 II (outer)
Powder injectors	Oerlikon Twin 150
Powder	œrlikon metco, metcoclad 316L-Si, 106 ± 45µm
6-axis Robot	Staubli RX160
Carrier gas	Argon
RGB camera	Precitec ZO YW30 CAM90° YW50 660

Table 8 details the parameters employed in the experiments. Experiment 1 (Exp-1) and Experiment 2 (Exp-2) maintain identical line energy, calculated as the ratio of laser power to scanning speed. Similarly, all experiments maintain the same powder deposition rate, calculated as the powder feed rate divided by the scanning speed, at approximately 0.015 g/mm. Currently, in-situ measurements for mass/enthalpy/momentum of powder flow are unavailable. As a result, only two experiments have been conducted to assess the efficiency of both the classical ALE method and the proposed model for the same benchmark.

Table 8: Fabrication parameters used in experiments.

Label	Laser power	Scanning speed	Powder feed rate	Carrier gas rate
-	W	mm/s	g/min	L/min
Exp-1	250	10	6.8	6
Exp-2	350	14.1	9.6	6

3.2.2. Numerical model set-up

Figure 14 shows the geometry and some basic dimensions of the mesh. The experimental results indicate that the melting pool size stabilizes after a printing length of 5 mm. To reduce computational costs, a mesh with a length of 10 mm has been prepared for the simulations. Symmetry conditions are also applied to further reduce the mesh size, with the smallest element dimensions being approximately 100 µm (y direction) × 100 µm (x direction) × 6 µm (z direction).

Table 9 shows the material properties of 316L employed in the numerical models. The melting temperature is 1450 ℃, and a positive gradient of surface tension has been used in the current study.

Table 9: Material properties of 316L stainless steel used in this model [45, 46, 47].

Parameters	20 °C	1400 °C	1450 °C	2800 °C
Thermal conductivity [W/mK]	14.7	28.3	28.3	28.3
Specific enthalpy [kJ/kg]	0	831.5	1165.4	2062.24
Density [kg/m^3]	8000	7300	7300	7300
Dynamic viscosity [Pa s]	1000	1000	0.007	0.007
Surface tension [N/m]	-	1.50	1.51	1.83

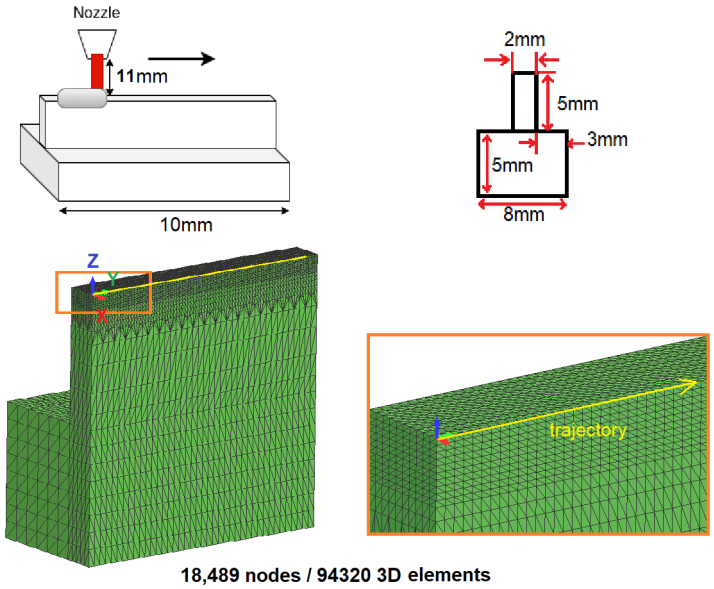

Figure 14: Schematic representation of geometry and its dimensions.

For the fiber laser, the intensity of laser power is generally described by a Gaussian function using the same formulation (Eq. 20). The diameter of the laser beam (1.4 mm) has been measured experimentally. Since the laser power intensity after attenuation caused by the powder stream is not measured in this study, a small value of the Gaussian function parameter (B) is used to approximate the laser attenuation effect. The absorptivity value is calibrated numerically to obtain the same melting pool width. Table 10 provides the laser power parameters.

Table 10: Parameters of heat source.

Power (P)	Radius (R)	Absorptivity (η)	Gaussian function (B)
Watt	mm	-	-
250/350	0.7	0.45	1

In the current model, the powder-related parameters (powder concentration, enthalpy due to the laser-powder interaction, momentum related to the powder deposition) should be measured or calculated/calibrated before the simulations. These powder-related parameters serve as the inputs for the proposed model. The powder concentration can be fitted by a Gaussian

distribution, which can be expressed by:

$$\dot{a}(r) = \frac{B * \dot{m}}{\pi * r_s^2} * e^{(-B * \frac{r^2}{r_s^2})} \tag{22}$$

with $B = 2.0$ for EXP-1 and 1.2 for EXP-2, $r_s = 1$ mm. $\dot{m}$ is the mass deposition rate shown in Table 10.

Turning now to the definition of momentum associated with powder flow, we consider that powder particles have the same speed as the carrier gas. Therefore, the velocity of powder particle is expressed as:

$$|v_{\mathrm{p}}| = \frac{V_{\mathrm{gas}}}{\pi * (R_{\mathrm{ext}}^2 - R_{\mathrm{int}}^2)} \tag{23}$$

where V_{gas} is the debit of gas ($\mathrm{L} \cdot \mathrm{min}^{-1}$); R_{ext} (7 mm) and R_{int} (6.5 mm) are the radius of external and internal nozzle. For simplifying the definition of velocity field, all the particles are supposed to have the same value, approximately equal to $V_{\mathrm{z}} = -|v_{\mathrm{p}}| * cos(\theta)$ where θ is the angle between speed vector and axis z (see Figure 14).

Similar to the powder concentration, the temperature of powder particles can depend on the distance to the centre of deposition and travailing trajectory. In the current study, a Gaussian distribution is employed to describe the temperature distribution is space:

$$T(r) = C * T(0) * e^{(-C * \frac{r^2}{r_T^2})} \tag{24}$$

where C, r_T and $T(0)$ are parameters to define temperature distribution. In the current study, $T(0) = 1000$ °C, $C = 1.1$ and $r_T = 1$ mm are used.

3.2.3. Comparisons of results

Figure 15 shows the temperature distribution and velocity field. Thanks to the MTF framework, the thermal-fluid problem is solely performed in a small zone containing the melting pool, where the velocity field is presented. The MTF framework can considerably accelerate the simulation without reducing the precision of the numerical solution. A time step of $2*10^{-4}$ s is employed for all the simulations. Both the classical ALE model and the improved ALE model are used to model the same problem. Thanks to the MTF framework, the proposed improved ALE model is approximately two times more efficient than the classical ALE model, highlighting the enhanced computational efficiency of the proposed model.

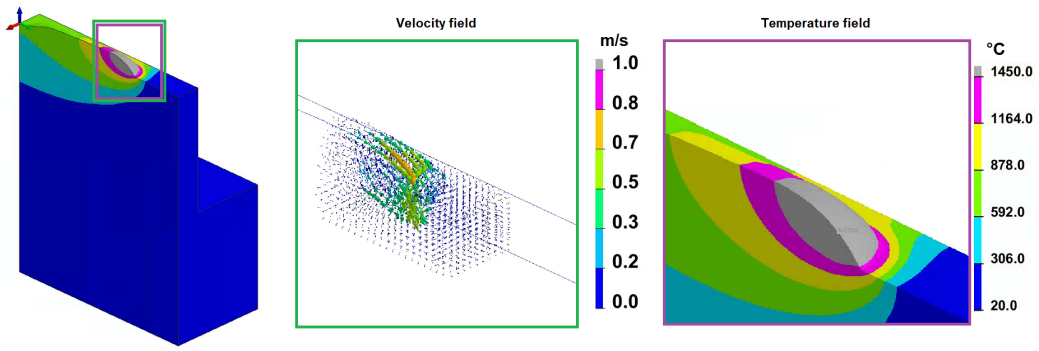

Figure 15: Temperature distribution and velocity field.

Compared to the improved ALE method, the classical ALE method utilizes the same powder concentration parameters (Eq. 22) and heat source parameters (Table 10). The key distinction lies in the fact that the improved ALE method incorporates the enthalpy and momentum associated with the powder flux, while all the other parameters remain the same. Compared to the classical ALE method, the improved ALE method introduces new input parameters into the model, resulting in more physically accurate simulations with the possibility of finer control.

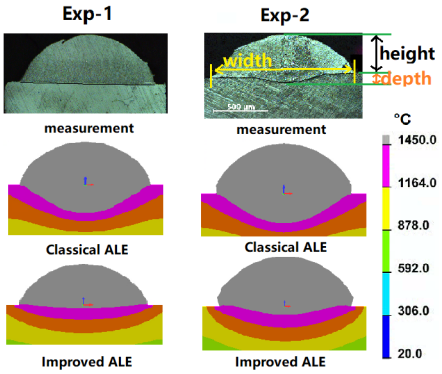

Comparison of melting pool size ex-situ by micoscope

Label	type analysis	height (mm)		width (mm)		depth (mm)	
		value	deviation	value	deviation	value	deviation
Exp-1	measurement	0.46	--	1.24	--	0.01	--
	Classical ALE	0.57	0.11 (23.9%)	1.48	0.24 (19.3%)	0.352	0.342 (34.2)
	Improved ALE	0.44	0.02 (-4.3%)	1.20	-0.04 (-3.2%)	0.006	-0.004 (-40%)
Exp-2	measurement	0.42	--	1.32	--	0.07	--
	Classical ALE	0.59	0.17 (40.5%)	1.52	0.20 (15.2%)	0.32	0.25 (3.57)
	Improved ALE	0.46	0.04 (8.7%)	1.40	0.08 (6.1%)	0.08	0.01 (14.3%)

Figure 16: Melting pool size observed in ex-situ measurements and simulations.

Figure 16 illustrates the shape of the melting pool measured and simulated after solidification, with the melting pool dimensions provided in the table. The deviation represents the difference between the simulated and measured dimensions. A symmetry condition is used to reproduce the com-

plete fusion profile. The comparisons confirm that the improved ALE method enables better simulation of the DED process by considering the effects (enthalpy, momentum) of the powder flux, showing excellent agreement with the experiments. In contrast, the classical ALE method overestimates the melting pool size due to its oversimplifications.

Figure 17 illustrates the measured and simulated height of the track after cooling, offering insights into the evolution of the melt pool height as a function of printing distance. The comparison indicates that the improved ALE model provides a more accurate prediction of the height of the newly formed track compared to the classical ALE model. Furthermore, both ALE models demonstrate a smooth prediction of the track's height, while the experimental measurements show oscillations, likely attributed to the presence of non-melted powder particles and measurement noise.

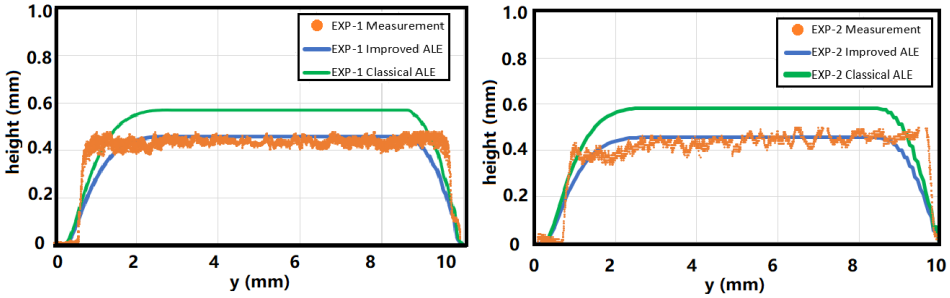

Figure 17: height of new formed track in printing direction.

Turning to the comparison of melting pool size during the process, the melting pool length and width are captured in-situ by the RGB camera. Figure 18 presents the comparisons of the melting pool observed in-situ and simulated. Generally, a good correlation of melting pool size has been observed for both the Classical ALE and Improved ALE methods. Compared to ex-situ measurements (1.24 mm in Exp-1 and 1.32 mm in Exp-2), it is noteworthy that the in-situ measurements (1.26 $\pm$ 0.2 mm in Exp-1 and 1.32 $\pm$ 0.2 mm in Exp-2) have almost same estimation of the melting pool width, which confirms the camera gives good measurements. The melting pool width/length confirms that the improved ALE method provides better predictions in both cases. The melting pool size predicted by the Classical ALE tends to be consistently overestimated compared to the measurements due to its oversimplifications.

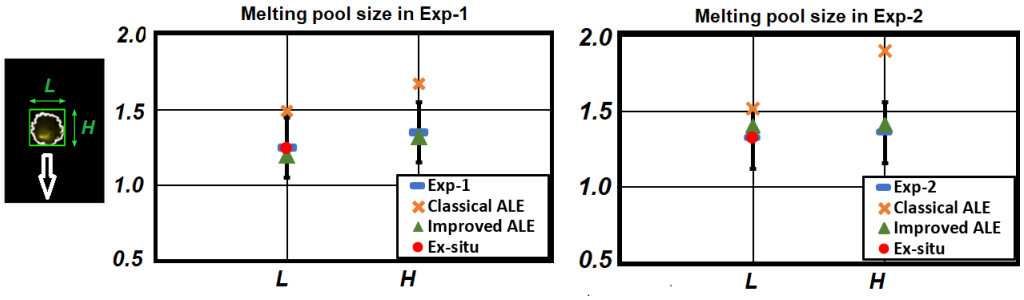

Figure 18: Melting pool size observed in in-situ measurements and simulations.

According to the aforementioned comparisons of melt pool size (in-situ and ex-situ), the improved ALE model demonstrates better accuracy in predicting the melt pool size across all cases compared to the classical ALE model, thus confirming the fidelity and improved performance of the proposed model.

4. Conclusions and perspectives

In this study, we introduced an improved ALE method for DED simulation, applying the MTF framework to accelerate the simulations. Compared to the classical ALE method, the improved ALE approach considers the effects of powder (mass, enthalpy, momentum) on melting pool simulation, which requires more input parameters, resulting in a more physically accurate and predictive simulation. The proposed model provides the possibility of more controlling of the simulation, which gives better correlation with the experiments. The proposed ALE model is not as sophistic as multi-phase CFD models that model directly powder particles, while it strikes a balance, providing a good compromise between the finer resolution of multi-phase CFD models and the classical over-simplified ALE model.

The first application with the fixed nozzle shows that the variation of temperature and momentum of powder particles can impact the melt pool size. The parameters of powder concentration have an signification effect on the final melt pool shape. The momentum/enthalpy depend on both velocity/temperature of the powder and the mass absorbed rate by the melting pool.

The second application in DED simulation shows the efficiency of proposed model in simulating the real engineering case. The classical ALE

method has over-estimated the melting pool size, especially the depth, due to its non-physical assumptions and simplifications. The improved ALE method has successfully predicted the melting pool size.

The future developments concerns firstly development of experimental measurements or numerical methods (finite volume method coupled with discrete element method) for calculation powder-related parameters (powder distribution, velocity, temperature). Secondly, a static refined mesh is employed for the entire melted zone in the current study, which is computational cost. Therefore, it is possible to use the adaptive mesh refinement (AMR) technique [48] to accelerate the simulation, especially for large-scale geometry. Additional diagnostic tools should be developed and utilized to obtain more experimental data, which will provide stronger support for validating and enhancing the numerical results.

5. Acknowledgement

The authors would like to thank Carnot Institute I@L for its financial support as part of the Tortellini project.

References

[1] K. Shah, A. J. Pinkerton, A. Salman, L. Li, Effects of melt pool variables and process parameters in laser direct metal deposition of aerospace alloys, Materials and Manufacturing Processes 25 (12) (2010) 1372–1380. arXiv:https://doi.org/10.1080/10426914.2010.480999, doi:10.1080/10426914.2010.480999.
URL https://doi.org/10.1080/10426914.2010.480999

[2] A. J. Pinkerton, L. Li, An investigation of the effect of pulse frequency in laser multiple-layer cladding of stainless steel, Applied Surface Science 208-209 (2003) 405–410, physics and Chemistry of Advanced Laser Materials Processing. doi:https://doi.org/10.1016/S0169-4332(02)01420-4.
URL https://www.sciencedirect.com/science/article/pii/S0169433202014204

[3] S. Li, H. Xiao, K. Liu, W. Xiao, Y. Li, X. Han, J. Mazumder, L. Song, Melt-pool motion, temperature variation and dendritic morphology of inconel 718 during pulsed- and continuous-wave laser additive manufacturing: A comparative study, Materials & Design 119 (2017)

351–360. doi:https://doi.org/10.1016/j.matdes.2017.01.065.
URL https://www.sciencedirect.com/science/article/pii/S0264127517300849

[4] L. Jegou, J. Lachambre, N. Tardif, M. Guillemot, A. Dellarre, A. Zaoui, T. Elguedj, V. Kaftandjian, N. Beraud, Bichromatic melt pool thermal measurement based on a red, green, and blue camera: Application to additive manufacturing processes, Optics & Laser Technology 167 (2023) 109799. doi:https://doi.org/10.1016/j.optlastec.2023.109799.
URL https://www.sciencedirect.com/science/article/pii/S0030399223006928

[5] A. J. Pinkerton, Advances in the modeling of laser direct metal deposition, Journal of Laser Applications 27 (S1) (2015) S15001. arXiv:https://doi.org/10.2351/1.4815992, doi:10.2351/1.4815992.
URL https://doi.org/10.2351/1.4815992

[6] P. Michaleris, Modeling metal deposition in heat transfer analyses of additive manufacturing processes, Finite Elements in Analysis and Design 86 (2014) 51–60. doi:https://doi.org/10.1016/j.finel.2014.04.003.
URL https://www.sciencedirect.com/science/article/pii/S0168874X14000584

[7] C. Bonacina, G. Comini, A. Fasano, M. Primicerio, Numerical solution of phase-change problems, International Journal of Heat and Mass Transfer 16 (10) (1973) 1825–1832. doi:https://doi.org/10.1016/0017-9310(73)90202-0.
URL https://www.sciencedirect.com/science/article/pii/0017931073902020

[8] A. M. Kamara, W. Wang, S. Marimuthu, L. Li, Modelling of the melt pool geometry in the laser deposition of nickel alloys using the anisotropic enhanced thermal conductivity approach, Proceedings of the Institution of Mechanical Engineers, Part B: Journal of Engineering Manufacture 225 (1) (2011) 87–99. arXiv:https://doi.org/10.1177/09544054JEM2129, doi:10.1177/09544054JEM2129.
URL https://doi.org/10.1177/09544054JEM2129

[9] K.-H. Lee, G. J. Yun, A novel heat source model for analysis of melt pool evolution in selective laser melting process, Additive Manufacturing 36 (2020) 101497. doi:https://doi.org/10.1016/j.addma.2020.101497.
URL https://www.sciencedirect.com/science/article/pii/S2214860420308691

[10] Y. Jia, Y. Saadlaoui, J.-M. Bergheau, A temperature-dependent heat source for simulating deep penetration in selective laser melting process, Applied Sciences 11 (23) (2021). doi:10.3390/app112311406.
URL https://www.mdpi.com/2076-3417/11/23/11406

[11] Y. Jia, Y. Saadlaoui, J.-C. Roux, J.-M. Bergheau, Steady-state thermal model based on new dedicated boundary conditions – application in the simulation of laser powder bed fusion process, Applied Mathematical Modelling 112 (2022) 749–766. doi:https://doi.org/10.1016/j.apm.2022.08.013.
URL https://www.sciencedirect.com/science/article/pii/S0307904X22003961

[12] M. Sussman, P. Smereka, S. Osher, A level set approach for computing solutions to incompressible two-phase flow, Journal of Computational Physics; (United States) (9 1994). doi:10.1006/jcph.1994.1155.
URL https://www.osti.gov/biblio/7075774

[13] L. Han, K. Phatak, F. Liou, Modeling of laser cladding with powder injection, Metallurgical and Materials Transactions B 35 (2004) 1139–1150.

[14] C. Hirt, B. Nichols, Volume of fluid (vof) method for the dynamics of free boundaries, Journal of Computational Physics 39 (1) (1981) 201–225. doi:https://doi.org/10.1016/0021-9991(81)90145-5.
URL https://www.sciencedirect.com/science/article/pii/0021999181901455

[15] M. Bayat, V. K. Nadimpalli, F. G. Biondani, S. Jafarzadeh, J. Thorborg, N. S. Tiedje, G. Bissacco, D. B. Pedersen, J. H. Hattel, On the role of the powder stream on the heat and fluid flow conditions during directed energy deposition of maraging steel—multiphysics modeling and experimental validation, Additive Manufacturing 43 (2021) 102021. doi:https://doi.org/10.1016/j.addma.2021.102021.
URL https://www.sciencedirect.com/science/article/pii/S221486042100186X

[16] S. Lin, Z. Gan, J. Yan, G. J. Wagner, A conservative level set method on unstructured meshes for modeling multiphase thermo-fluid flow in additive manufacturing processes, Computer Methods in Applied Mechanics and Engineering 372 (2020) 113348. doi:https://doi.org/10.1016/j.cma.2020.113348.
URL https://www.sciencedirect.com/science/article/pii/S0045782520305338

[17] H. Wei, F. Liu, W. Liao, T. Liu, Prediction of spatio temporal variations of deposit profiles and inter-track voids during laser directed energy deposition, Additive Manufacturing 34 (2020) 101219. doi:https://doi.org/10.1016/j.addma.2020.101219.
URL https://www.sciencedirect.com/science/article/pii/S2214860420305911

[18] A. Aggarwal, A. Chouhan, S. Patel, D. Yadav, A. Kumar, A. Vinod, K. Prashanth, N. Gurao, Role of impinging powder particles on melt pool hydrodynamics, thermal behaviour and microstructure in laser-assisted ded process: A particle-scale dem – cfd – ca approach, International Journal of Heat and Mass Transfer 158 (2020) 119989. doi:https://doi.org/10.1016/j.ijheatmasstransfer.2020.119989.
URL https://www.sciencedirect.com/science/article/pii/S0017931019367997

[19] H. W. Mindt, O. Desmaison, M. Megahed, A. Peralta, J. Neumann, Modeling of Powder Bed Manufacturing Defects, Journal of Materials Engineering and Performance 27 (1) (2018) 32–43. doi:10.1007/s11665-017-2874-5.

[20] H. Hua, J. Shin, J. Kim, Level Set, Phase-Field, and Immersed Boundary Methods for Two-Phase Fluid Flows, Journal of Fluids Engineering 136 (2), 021301 (11 2013). arXiv:https://asmedigitalcollection.asme.org/fluidsengineering/article-pdf/136/2/021301/6190065/fe_136_02_021301.pdf, doi:10.1115/1.4025658.
URL https://doi.org/10.1115/1.4025658

[21] F. de Sousa, N. Mangiavacchi, L. Nonato, A. Castelo, M. Tomé, V. Ferreira, J. Cuminato, S. McKee, A front-tracking/front-capturing method for the simulation of 3d multi-fluid flows with free surfaces, Journal of Computational Physics 198 (2) (2004) 469–499. doi:https://doi.org/10.1016/j.jcp.2004.01.032.
URL https://www.sciencedirect.com/science/article/pii/S0021999104000488

[22] M.-J. Li, J. Chen, Y. Lian, F. Xiong, D. Fang, An efficient and high-fidelity local multi-mesh finite volume method for heat transfer and fluid flow problems in metal additive manufacturing, Computer Methods in Applied Mechanics and Engineering 404 (2023) 115828. doi:https://doi.org/10.1016/j.cma.2022.115828.
URL https://www.sciencedirect.com/science/article/pii/S0045782522007848

[23] S. Morville, M. CARIN, P. Peyre, M. Gharbi, D. CARRON, P. LE MASSON, R. Fabbro, 2d longitudinal modeling of heat transfer and fluid flow during multilayered direct laser metal deposition process, Journal of Laser Applications 24 (3) (2012) 1–9, version post-print de l'article : JLA Vol : 24 Iss:3. 2D longitudinal modeling of heat transfer and fluid flow during multilayered direct laser metal deposition process.
URL https://hal.archives-ouvertes.fr/hal-00799208

[24] A. Kumar, S. Roy, Effect of three-dimensional melt pool convection on process characteristics during laser cladding, Computational Materials Science 46 (2) (2009) 495–506. doi:https://doi.org/10.1016/j.commatsci.2009.04.002.
URL https://www.sciencedirect.com/science/article/pii/S0927025609001608

[25] F. Wirth, K. Wegener, A physical modeling and predictive simulation of the laser cladding process, Additive Manufacturing 22 (2018) 307–319. doi:https://doi.org/10.1016/j.addma.2018.05.017.
URL https://www.sciencedirect.com/science/article/pii/S2214860418301349

[26] Z. Gan, G. Yu, X. He, S. Li, Surface-active element transport and its effect on liquid metal flow in laser-assisted additive manufacturing, International Communications in Heat and Mass Transfer 86 (2017) 206–214. doi:https://doi.org/10.1016/j.icheatmasstransfer.2017.06.007.
URL https://www.sciencedirect.com/science/article/pii/S0735193317301409

[27] Y. Jia, Y. Saadlaoui, E. Feulvarch, J.-M. Bergheau, An efficient local moving thermal-fluid framework for accelerating heat and mass transfer simulation during welding and additive manufacturing processes, Computer Methods in Applied Mechanics and Engineering 419 (2024) 116673. doi:https://doi.org/10.1016/j.cma.2023.116673.
URL https://www.sciencedirect.com/science/article/pii/S004578252300796X

[28] Z. Gan, G. Yu, X. He, S. Li, Numerical simulation of thermal behavior and multicomponent mass transfer in direct laser deposition of co-base alloy on steel, International Journal of Heat and Mass Transfer 104 (2017) 28–38. doi:https://doi.org/10.1016/j.ijheatmasstransfer.2016.08.049.
URL https://www.sciencedirect.com/science/article/pii/S0017931016310377

[29] W. Jiazhu, T. Liu, H. Chen, F. Li, H. Wei, Y. Zhang, Simulation of laser attenuation and heat transport during direct metal deposition considering beam profile, Journal of Materials Processing Technology 270 (2019) 92–105. doi:https://doi.org/10.1016/j.jmatprotec.2019.02.021.
URL https://www.sciencedirect.com/science/article/pii/S0924013619300779

[30] X. Guan, Y. F. Zhao, Numerical modeling of coaxial powder stream in laser-powder-based directed energy deposition process, Additive Manufacturing 34 (2020) 101226. doi:https://doi.org/10.1016/j.addma.2020.101226.
URL https://www.sciencedirect.com/science/article/pii/S2214860420305984

[31] S. Wen, Y. Shin, J. Murthy, P. Sojka, Modeling of coaxial powder flow for the laser direct deposition process, International Journal of Heat and Mass Transfer 52 (25) (2009) 5867–5877. doi:https://doi.org/10.1016/j.ijheatmasstransfer.2009.07.018.
URL https://www.sciencedirect.com/science/article/pii/S0017931009004517

[32] Y. Jia, H. Naceur, Y. Saadlaoui, L. Dubar, J. Bergheau, A comprehensive comparison of modeling strategies and simulation techniques applied in powder-based metallic additive manufacturing processes, Journal of Manufacturing Processes 110 (2024) 1–29. doi:https://doi.org/10.1016/j.jmapro.2023.12.048.
URL https://www.sciencedirect.com/science/article/pii/S1526612523011568

[33] Z. Liu, H.-C. Zhang, S. Peng, H. Kim, D. Du, W. Cong, Analytical modeling and experimental validation of powder stream distribution during direct energy deposition, Additive Manufacturing 30 (2019) 100848. doi:https://doi.org/10.1016/j.addma.2019.100848.
URL https://www.sciencedirect.com/science/article/pii/S2214860419302143

[34] Z. Jardon, P. Guillaume, J. Ertveldt, M. Hinderdael, G. Arroud, Offline powder-gas nozzle jet characterization for coaxial laser-based directed energy deposition, Procedia CIRP 94 (2020) 281–287, 11th CIRP Conference on Photonic Technologies [LANE 2020]. doi:https://doi.org/10.1016/j.procir.2020.09.053.
URL https://www.sciencedirect.com/science/article/pii/S2212827120312385

[35] Y. Saadlaoui, Éric Feulvarch, A. Delache, J.-B. Leblond, J.-M. Bergheau, A new strategy for the numerical modeling of a weld

pool, Comptes Rendus Mécanique 346 (11) (2018) 999–1017, computational methods in welding and additive manufacturing Simulation numérique des procédés de soudage et fabrication additive. doi:https://doi.org/10.1016/j.crme.2018.08.007.
URL https://www.sciencedirect.com/science/article/pii/S1631072118301761

[36] O. Desmaison, M. Bellet, G. Guillemot, A level set approach for the simulation of the multipass hybrid laser/gma welding process, Computational Materials Science 91 (2014) 240–250. doi:10.1016/j.commatsci.2014.04.036.

[37] Y. Zhang, Q. Chen, G. Guillemot, C.-A. GANDIN, M. Bellet, Numerical modelling of fluid and solid thermomechanics in additive manufacturing by powder-bed fusion: Continuum and level set formulation applied to track- and part-scale simulations, Comptes Rendus Mecanique (09 2018). doi:10.1016/j.crme.2018.08.008.

[38] Q. Chen, G. Guillemot, C.-A. Gandin, M. Bellet, Numerical modelling of the impact of energy distribution and marangoni surface tension on track shape in selective laser melting of ceramic material, Additive Manufacturing 21 (2018) 713–723. doi:https://doi.org/10.1016/j.addma.2018.03.003.
URL https://www.sciencedirect.com/science/article/pii/S2214860417304670

[39] W. Dettmer, D. Perić, A computational framework for free surface fluid flows accounting for surface tension, Computer Methods in Applied Mechanics and Engineering 195 (23) (2006) 3038–3071, incompressible CFD. doi:https://doi.org/10.1016/j.cma.2004.07.057.
URL https://www.sciencedirect.com/science/article/pii/S0045782505002380

[40] P. H. Saksono, D. Perić, On finite element modelling of surface tension Variational formulation and applications Part I: Quasistatic problems, Computational Mechanics 38 (3) (2006) 265–281. doi:10.1007/s00466-005-0747-5.

[41] J.-B. Leblond, T. Sayet, J.-M. Bergheau, On the incorporation of surface tension in finite-element calculations, Comptes Rendus Mecanique 341 (2013) 770–775.

[42] ESI-Group, Software sysweld version 2023, Lyon, France (2023).

[43] ESI-Group, Visual-environment 18.0, Lyon, France (2022).

[44] Y. Jia, Y. Saadlaoui, H. Hamdi, J. Sijobert, J.-C. Roux, J.-M. Bergheau, An experimental and numerical case study of thermal and mechanical consequences induced by laser welding process, Case Studies in Thermal Engineering 35 (2022) 102078. doi:https://doi.org/10.1016/j.csite.2022.102078.
URL https://www.sciencedirect.com/science/article/pii/S2214157X22003240

[45] G. Knapp, T. Mukherjee, J. Zuback, H. Wei, T. Palmer, A. De, T. DebRoy, Building blocks for a digital twin of additive manufacturing, Acta Materialia 135 (2017) 390–399. doi:https://doi.org/10.1016/j.actamat.2017.06.039.
URL https://www.sciencedirect.com/science/article/pii/S1359645417305141

[46] T. Heeling, M. Cloots, K. Wegener, Melt pool simulation for the evaluation of process parameters in selective laser melting, Additive Manufacturing 14 (2017) 116–125. doi:https://doi.org/10.1016/j.addma.2017.02.003.
URL https://www.sciencedirect.com/science/article/pii/S221486041630313X

[47] H. Fukuyama, H. Higashi, H. Yamano, Thermophysical properties of molten stainless steel containing 5 mass % b4c, Nuclear Technology 205 (9) (2019) 1154–1163. arXiv:https://doi.org/10.1080/00295450.2019.1578572, doi:10.1080/00295450.2019.1578572.
URL https://doi.org/10.1080/00295450.2019.1578572

[48] F. Yang, A. Rassineux, C. Labergere, K. Saanouni, A 3d h-adaptive local remeshing technique for simulating the initiation and propagation of cracks in ductile materials, Computer Methods in Applied Mechanics and Engineering 330 (2018) 102–122. doi:10.1016/j.cma.2017.10.012.